Direct 2,3-butanediol conversion to butene-rich C_{3+} olefins over Cu modified 2D pillared MFI: consequence of reduced diffusion length

Shiba Adhikari[1,#], Junyan Zhang[1,2,#], Kinga Unocic[1], Evan C. Wegener[3], Pranaw Kunal[1], Dhruba J. Deka[1], Todd Toops[1], Sreshtha Sinha Majumdar[1], Theodore R. Krause[3], Dongxia Liu[2], Zhenglong Li[1,]*

[1] Oak Ridge National Laboratory, Oak Ridge, TN 37830, USA

[2] University of Maryland, College Park, MD 20742, USA

[3] Argonne National Laboratory, Lemont, IL 60439, USA

Corresponding Author

*Correspondence to: liz3@ornl.gov

Keywords: 2,3-Butanediol; Butene; 2D zeolite; Sustainable aviation fuels; Diffusion free; Decarbonization

Abstract

2,3-Butanediol (2,3-BDO), a critical C_4 platform chemical derived from biomass, syngas, or CO_2, can be converted to C_{3+} olefins, serving as important renewable feedstocks for producing sustainable aviation fuels to decarbonize the hard-to-electrify air transportation sector. Herein, we report a bifunctional Cu modified diffusion-free 2D pillared MFI catalyst (Cu/PMFI) which can selectively catalyze 2,3-BDO conversion to butene-rich C_{3+} olefins (95% selectivity at 97% conversion, 523 K). 2,3-BDO conversion to butenes over Cu/PMFI primarily occurs via methyl ethyl ketone intermediate while 2-methyl propanal is also observed as another minor dehydration product that leads to butene formation. In comparison with a control mesoporous Cu/ZSM-5 sample prepared by the post-synthetic approach, Cu/PMFI shows favorable C_{3+} olefin selectivity (95% over Cu/PMFI vs 80% over Cu/ZSM-5 at ~5.1 h TOS). The coke formation over Cu/PMFI is dramatically suppressed by >50% in contrast to Cu/ZSM-5 in 90 hours' 2,3-BDO conversion due to the reduced diffusion length. Cu/PMFI also favors butene formation and minimize non-butene C_{3+} olefins by inhibiting the downstream oligomerization and cracking reactions. This study highlights the usefulness of the diffusion-free 2D PMFI materials in catalytic conversion of biomass-derived platform molecules and significance of diffusion impact on catalyst coke formation and product distributions.

Introduction

Over the last few decades, there is an increasing demand for olefins, with most produced from crude oil and natural gas in the petrochemical industry. It was estimated that 400 million tons of light olefins (ethylene, propylene, butenes, and butadiene) are produced annually via different processes like fluid catalytic cracking, steam cracking, and dehydrogenation[1]. Besides the widely produced and used ethylene, C_{3+} olefins, such as butenes, are in growing demand, serving as important commodity chemicals and critical feedstocks for middle-distillate fuel production, such as aviation fuels. The feedstock shift from naphtha to shale gas has led to primarily ethylene production, creating a strong need for on-purpose C_{3+} olefin production. More importantly, increasing concerns about climate change have led to active searching for alternative approaches in the production of these olefins from renewable carbon sources, such as biomass. Renewable C_{3+} olefins become critical feedstocks for synthesizing sustainable aviation fuels to address the greenhouse gas emission reduction challenges for the aviation sector, one of the most-difficult-to-decarbonize tasks.

Several pathways have been developed to convert various biomass-derived platform chemicals to C_{3+} olefins. Biomass-derived γ-valerolactone (GVL) has been identified as an important platform molecule to make butenes via ring-opening and decarboxylation reactions, where various solid acid catalysts have been studied, including heteroatom modified zeolites[2], Ni_2P/MCM-41[3], and amorphous SiO_2/Al_2O_3[4]. Biomass fermentation-derived ethanol, another useful platform chemical, has been studied extensively to synthesize butenes over zeolite catalysts[5, 6]. Other biomass-derived small platform chemicals, such as 1-propanol[7], 1-butanol[8], and acetone[9], are also good candidates for synthesizing propene and butenes. Besides these opportunities, 2,3-butanediol (2,3-BDO) is another important C_4 platform chemical, which has recently received significant interests because of its potential to be synthesized in a high titer owing to its low toxicity to producing microorganisms[10]. This molecule has been prepared from several readily available resources including lignocellulosic biomass as well as syngas and CO_2 [10, 11]. It can be used to produce butenes[12,13], and to make aviation biofuels after further oligomerization, which has been demonstrated by our team[14].

Conversion of 2,3-BDO to butene-rich C_{3+} olefins requires bifunctional catalysts with both hydrogenation (e.g., Cu) and dehydration sites (e.g., Brønsted acids) to form butenes in one process step, where Cu modified porous aluminosilicate-type materials (e.g., Cu/ZSM-5, Cu/Al-MCM-48, and Cu/Al-SBA-15) have been studied[12, 13]. Cu modified microporous H-ZSM-5 catalysts were demonstrated for selective butene formation over 19 wt% CuO/ZSM-5 (SiO_2/Al_2O_3=280) at 523 K, where the balance of Cu sites and acid sites is important for optimum butene production[12]. Coke formation was identified as one of the major deactivation mechanisms for 2,3-BDO conversion over these microporous Cu/ZSM-5 catalysts. In order to address the coking challenge, mesopores were introduced into conventional H-ZSM-5 by post-synthetic alkaline treatment methods[15] to slow down the coke formation[13, 16, 17]. Besides the mesopore volumes, the interconnectivity of mesopore channels is another critical factor to consider for mitigating coke formation and optimizing product distributions. H-ZSM-5 mesopores generated via the post-synthetic alkaline treatment methods are usually still largely connected via micropores[18], thus there are opportunities for further reducing the diffusion constraints by developing hierarchical MFI zeolites with improved mesopore interconnectivity. The soft-template mesoporogendirected hierarchical zeolite synthesis approach can generate a multilamellar mesoporous MFI structure with a dual-porogenic template comprising a multiple quaternary ammonium head and a hydrophobic alkyl chain tail[19]. After silica pillaring, a 2D pillared MFI (PMFI) zeolite can be obtained, which possesses ordered mesopore structures between MFI nanosheets[20]. This type of zeolite is known to be diffusion free[21] (~1 nm diffusion length) due to the nano size thickness (~3.2 nm[22]) and well-established mesopore interconnectivity[23], which offers opportunities to further address the coke formation issue. Unfortunately, currently there is no reported work on developing PMFI-based catalysts for 2,3-BDO conversion to butenes (or butene-rich C_{3+} olefins) and it is intriguing to study the impact of reduced diffusion path length on product distributions and coke formation.

In this study, we report a Cu modified 2D pillared MFI (Cu/PMFI) for 2,3-BDO conversion to butene-rich C_{3+} olefins. This catalyst was characterized to understand the physical/chemical properties, Cu site distributions/species as well as acid sites via various characterizations, such as scanning transmission electron microscopy (STEM), X-ray absorption spectroscopy (XAS), and pyridine diffuse reflectance infrared Fourier transform spectroscopy (DRIFTS). The catalyst performance for butene-rich olefin production and reaction condition optimizations over Cu/PMFI were discussed. Cu modified mesoporous H-ZSM-5 catalyst synthesized via ammonia evaporation method was employed as a reference to compare with Cu/PMFI to demonstrate the impact of diffusion length on coke formation and product distributions.

Experimental

Materials. Tetraethyl orthosilicate (TEOS, 98%), sodium hydroxide (NaOH, ≥ 97.0%), sulfuric acid (H_2SO_4, 95.0-98.0%), aluminium isopropoxide (98%), tetrabutylammonium hydroxide solution (TPAOH, 40 wt% in H_2O), ammonium nitrate (NH_4NO_3, ⩾99.0%), copper nitrate hexahydrate (99%), 2,3-butanediol (98%), ammonia solution (28.0–30.0% NH_3 basis) were purchased from Sigma Aldrich and used without any further purification unless otherwise stated. Diquaternary ammonium surfactant ($[C_{22}H_{45}\text{-}N^{+}(CH_3)_2\text{-}C_6H_{12}\text{-}N^{+}(CH_3)_2\text{-}C_6H_{13}]Br_2^{-}$, ($C_{22\text{-}6\text{-}6}$)) was synthesized based on the reported method[19].

Catalyst Preparation. Microporous ZSM-5 was synthesized by a hydrothermal synthesis method with composition of $100SiO_2/0.5Al_2O_3/20TPAOH/3000H_2O$. Firstly, 0.2 g aluminium isopropoxide was dissolved in 46 g DI water and 9.8 g 40 wt% TPAOH solution under stirring at 500 rpm. Then 20 g TEOS was added dropwise into the solution and the mixture was stirred in an ice bath at 500 rpm for 72 h. The obtained gel was transferred into autoclaves and heated to 443 K under rotation for 48 h. The solid zeolite was centrifuged, washed, and dried at 353 K overnight.

The pillared MFI was synthesized from the multilamellar MFI zeolites as reported by Choi et al[19]. Typically, a base solution was prepared by dissolving 8.0 g NaOH in 35.1 g DI water while an acid solution was made by adding 2.7 g H_2SO_4 into 48.0 g DI water. Then, the acid and basic solutions were mixed under vigorous magnetic stirring. 1.2 g $Al_2(SO_4)_3 \cdot 16H_2O$ was added into the solution followed by adding 37.6 g TEOS dropwise. The formed sol gel was stirred for 24 h at room temperature. Afterwards, 13.1 g $C_{22\text{-}6\text{-}6}$ was dissolved in 90.0 g DI water at 333 K and the obtained clear solution was added into the sol gel followed by continuous stirring for 2 h. The synthetic gel was transferred into

Teflon-lined stainless-steel autoclaves. The autoclaves were tumbled at 60 rpm and 423 K for five days. Finally, the sample was filtered, washed with DI water, and dried at 343 K overnight.

The pillaring process was performed by dispersing the multilamellar MFI in a TEOS solvent[20] at a weight ratio of TEOS to zeolite of 5 to 1. The suspension was heated at 351 K for 24 h under the protection of argon (Ar) atmosphere. The as-obtained powder was collected by filtering and was dried at room temperature overnight. Further hydrolysis was carried out by adding the sample into a NaOH aqueous solution (pH = 8) with solid to liquid weight ratio of 1 to 10. After stirring the mixture for 6 h at 313 K, the sample was centrifuged, washed with DI water, and then dried under ambient conditions. Finally, the sample was calcined at 723 K for 6 h under N_2 atmosphere (flow rate =1.7 cm^3 s^{-1}) and then under flowing air atmosphere (flow rate = 1.7 cm^3 s^{-1}) at 823 K for 12 h.

Cu loading on these catalysts was done by using the ammonia evaporation method with slight modification based on method reported in Zheng et al[12, 24]. Briefly, 0.76 g of copper nitrate was dissolved in 4 mL of water and the pH was adjusted to 9.1 by adding ammonia solution before making the final volume to 8 mL by adding deionized water. Then 1 g of proton form zeolite was added and stirred at room temperature for 4 h before stirring at 353 K for 2 h. After centrifuging and washing, the solid was dried overnight at 353 K before calcining it at 823 K for 4 h to obtain Cu modified catalysts.

Characterizations. The elemental composition was determined by inductively coupled plasma atomic emission spectroscopy (ICP-AES) at Galbraith Laboratories Inc (Knoxville, TN). Brunauer-Emmett-Teller (BET) surface areas and pore volumes were determined from nitrogen adsorption isotherms at 77 K using Autosorb-1 from Quantachrome Instruments. Before the measurement, the zeolite samples were degassed overnight at 573 K. Pore size distribution is calculated from the adsorption branch of N_2 isotherm based on nonlocal density functional theory (NLDFT). X-ray diffraction (XRD) measurements were collected on a PANalytical X-ray diffractometer using Cu-Kα radiation (λ=0.15418 nm).

The morphology and elemental distribution were analyzed by a scanning transmission electron microscopy (STEM) operated at 200 kV, equipped with an extreme field emission gun (X-FEG) electron source, high-angle annular dark-field (HAADF) detector, and Super-X energy-dispersive X-ray spectroscopy (EDX) system with 4 silicon-drift detectors (SDD) (Bruker XFlash 120 mm^2). The samples were prepared by both microtomes (Leica EM UC7) and drop cast methods.

XAS spectra were collected in transmission mode at the Cu K edge on the bending magnet beam line of the Materials Research Collaborative Access Team (MR-CAT) (Advanced Photon Source, Argonne National Laboratory). Energy calibration was performed simultaneously with sample measurements using a third ion chamber in series and a Cu metal foil. Before the XAS measurements, the catalyst was reduced under 3.5% H_2/He atmosphere at 573 K for 1 h. XAS spectra were analyzed with the Demeter software suite[25]. Standard procedures were used for performing normalization and background subtraction. The oxidation state of Cu was determined by comparing the normalized X-ray absorption near-edge structure (XANES) of the sample to known reference (Cu foil, Cu_2O, and CuO). The coordination parameters were determined by simultaneous fits in R-space of the magnitude of the k^1, k^2, and k^3-weighted extended X-ray absorption fine structure (EXAFS).

Pyridine adsorption DRIFTS measurements were performed using a Cary 600 Series FTIR spectrophotometer equipped with a mercury-cadmium-telluride (MCT) detector, and a Harrick Scientific Praying Mantis diffuse reflectance accessory. The spectra (32 scans) were collected using a hemispherical dome equipped with spectra-grade ZnSe windows from 4000-400 cm^{-1} with a 2 cm^{-1} resolution. Samples were pretreated by calcination at 773 K in 0.83 cm^3 s^{-1} 20% O_2/Ar flow for 1 h. Then the sample was cooled down to 573 K and flushed with 0.83 cm^3 s^{-1} Ar for 0.5 h to remove oxygen followed by reduction with 0.83 cm^3 s^{-1} 2% H_2/Ar for 1.5 h. After pretreatment, the sample was cooled down to 423 K under 0.83 cm^3 s^{-1} Ar 1 h to remove residual H_2. Before flowing pyridine, background spectrum was recorded under 0.83 cm^3 s^{-1} Ar. Then 0.17 cm^3 s^{-1} Ar was flown through a glass bubbler (room temperature) to carry pyridine vapor to the samples for pyridine adsorption until saturation. Following adsorption, 0.83 cm^3 s^{-1} Ar flow was used to purge the system to remove gas phase and physisorbed pyridine until the peak stabilized. The measurements were taken at 423 K under 0.83 cm^3 s^{-1} Ar flow.

Ammonia temperature programmed desorption (NH_3-TPD) measurements were performed using a Micromeritics AutoChem II 2090 chemisorption analyzer equipped with a Pfeiffer OmniStar quadrupole mass spectrometer. Approximately 0.04 g samples were loaded into the U-tube reactor and pretreated with similar procedure as the pyridine DRIFTS measurement. After cooling to 423 K, the catalyst was flushed with 0.83 cm^3 s^{-1} Ar flow for 1 h and then exposed to a flow of 1.66 cm^3 s^{-1} 1% NH_3 in Ar for 1.5 h. After purging with 0.83 cm^3 s^{-1} Ar flow for 3.5 h, desorption was performed at 0.17 K s^{-1} to 1073 K in 0.83 cm^3 s^{-1} Ar flow. The hydrogen temperature programmed reduction (H_2-TPR) was performed on the same instrument as the NH_3-TPD. Samples were pretreated by calcination at 773 K in 0.83 cm^3 s^{-1} 20% O_2/Ar flow for 1 h. Then the sample was cooled down to 323 K and flushed with 0.83 cm^3 s^{-1} Ar for 0.5 h to remove oxygen followed by temperature ramp to 673 K at 0.083 K s^{-1} with 0.17 cm^3 s^{-1} H_2 and 0.83 cm^3 s^{-1} Ar.

The thermogravimetric analysis (TGA) was completed using a TGA Q5000 (TA instrument, USA) to determine coke deposited on the samples during the reactions. The samples were heated to 573 K at 0.033 K s^{-1} and kept for 30 hours under Ar flow before cooling to 423 K and ramping up to 1173 K under air flow.

2,3-BDO conversion. Conversion of 2,3-BDO was carried out in a tubular quartz reactor (1/2" O.D.) with a fix-bed configuration under ambient pressure as described in our previous study[14]. Approximately 0.15 g catalyst was loaded in the quartz reactor and preheated at 573 K under H_2 (0.17 cm^3 s^{-1}) and Ar flow (0.83 cm^3 s^{-1}) and held at this temperature for 5400 s before changing to reaction temperatures. 2,3-BDO was fed into the reactor using a syringe pump (KD Scientific) along with hydrogen, and the products were analyzed with an on-line gas chromatograph equipped with a flame ionization detector (FID).

Results and discussion

Characterizations of H-PMFI and Cu/PMFI. Ammonia evaporation method was employed to introduce Cu sites onto H-PMFI (Si/Al=70), which generated Cu/PMFI with 13.9 wt% Cu loading based on ICP-AES analysis (Table 1). The XRD patterns of the as-synthesized H-PMFI and Cu/PMFI are consistent with the MFI topology (Figure S1), indicating this method of loading Cu does not change the crystallinity of the zeolite support. N_2 (77 K) adsorption-desorption isotherms (Figure S2) were measured to characterize the changes of the zeolites' textural properties before and after copper loading. H-PMFI has a typical Type IV isotherm, which indicates a hierarchically porous structure formed by pillaring 2D zeolite precursor[26]. After loading copper, the H4 hysteresis loop is preserved while N_2 uptake decreases in the relative pressure ranges related to both micropores and mesopores, and both micropore and mesopore volumes (normalized by sample weight) are shown to decrease significantly (Table 1). Pore volumes normalized by the weight of zeolite supports shows comparable values between H-PMFI and Cu/PMFI (Table S1), indicating the parent H-PMFI maintains the pore structure after Cu loading and decrease of pore volumes (normalized by sample weight) is mainly due to reduced wt% of PMFI within Cu/PMFI due to Cu introduction.

Table 1. Physical and chemical properties of H-PMFI and Cu/PMFI.

Sample	SAR	S_{total} $m^2\ g^{-1}$	V_{total} $cm^3\ g^{-1}$	V_{micro} $cm^3\ g^{-1}$	V_{meso} $cm^3\ g^{-1}$	Cu loading wt%
H-PMFI	70	814	0.57	0.13	0.44	-
Cu/PMFI	75	464	0.47	0.11	0.36	13.9

The surface area is determined by using the Brunauer, Emmett, and Teller (BET) method. Total pore volume is calculated by N_2 adsorption at P/P_o=0.95. Micropore volume is determined from the t-plot method. Mesopore volume is determined by subtracting micropore volume from total pore volume. SAR: Si/Al ratio.

HAADF STEM analysis along with EDX was performed to understand the morphology of Cu/PMFI and Cu distribution. Layered 2D MFI nanosheets were preserved after Cu loading as clearly observed in the STEM image (Figure 1(a)), and the interlayer spacing clearly shows the ordered mesopore structure, agreeing with the N_2 isotherm analysis. EDX mapping at low magnification confirms the presence of copper species over all the Cu/PMFI particles (Figure S3). HAADF STEM images of Cu/PMFI indicate the presence of Cu-containing nanoparticles, where both small (2-3 nm) and large (~20 nm) nanoparticles are observed (Figure 1(a-c)). These nanoparticles are mainly located on the external surfaces of zeolite particles, while some small nanoparticles also occupy the interlayer spacing (Figure 1(d)).

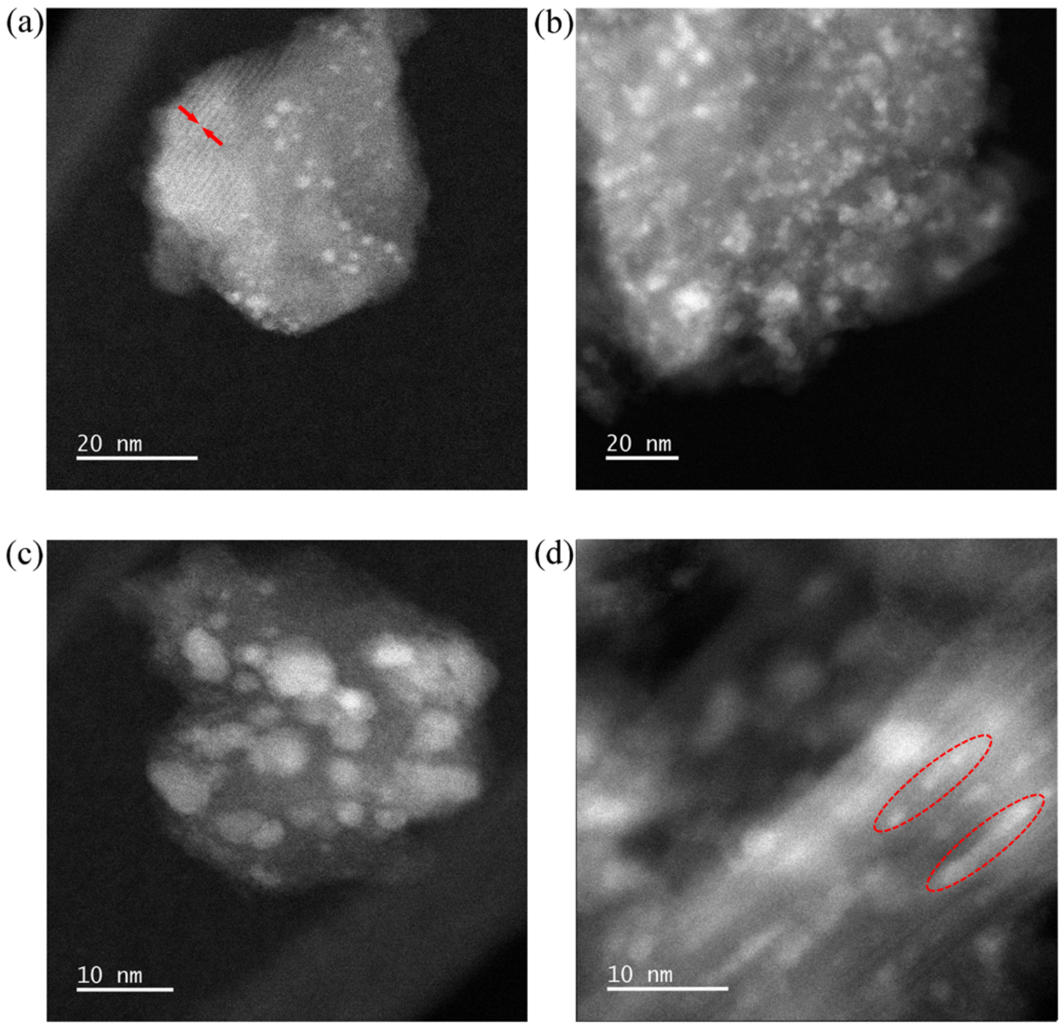

Figure 1. Microscopic study of Cu/PMFI after reduction under 16.9 kPa H_2 balanced with 84.4 kPa Ar at 573 K.

Besides the formation of Cu-containing nanoparticles, we also explored the possibility of forming other types of Cu sites (e.g., ion-exchanged Cu species) over Cu/PMFI, which has not been discussed in other Cu modified zeolites synthesized via the ammonia evaporation synthesis method[12]. H_2-TPR was first performed to understand the reducibility of different Cu species, where reduction of ion-exchanged Cu species was reported to occur at high temperatures (e.g., 663 K) while reduction of CuO nanoparticles to metallic Cu can be done at ~473 K[27]. H_2-TPR analysis of Cu/PMFI shows two reduction peaks with the primary peak at ~473 K and a minor peak at ~583 K (Figure S4), which likely suggests the presence of both CuO nanoparticles and ion-exchanged Cu species over the pre-reduced Cu/PMFI.

X-ray absorption spectroscopy was employed to further understand the copper species in Cu/PMFI (Figure 2). Prior to measurements, the sample was reduced at 573 K in 3.5% H_2/He and then cooled to room temperature to collect the spectrum. The XANES and EXAFS of the reduced catalyst and Cu foil and Cu_2O references are shown in Figure 2(a) and 2(b), respectively. The Cu species in reduced Cu/PMFI have similar edge energy as the Cu foil (8980.5 eV) as shown in the XANES spectrum, indicating a large fraction of Cu is in the metallic form, which is consistent with the H_2-TPR analysis. However, the white-line peak shape difference in XANES spectrum of the sample relative to the Cu foil suggests the presence of oxides, agreeing with the H_2-TPR analysis which shows at least two types of Cu species. The Cu(I) species broaden the characteristic peak around 8995 eV and lessen the split with the second peak around 9002 eV. The peak in the XANES of Cu/PMFI at 8984.0 eV is in the same position as the prominent feature in the Cu_2O spectrum, suggesting the oxide fraction is Cu(I). The EXAFS of the reduced Cu/PMFI sample shows a Cu-O peak at 1.4 Å and a Cu-Cu peak at 2.2 Å (phase uncorrected distances), consistent with a mixture of Cu oxide and metallic particles as indicated by the XANES. To estimate the fractions of Cu(0) and Cu(I) in the sample, a linear combination fit of the XANES was performed using the Cu foil and Cu_2O as references. Since the bulk foil is not a perfect reference for Cu nanoparticles and the Cu(I) fraction is very likely not bulk Cu_2O, only the leading edge of the XANES (-10 - 15 eV relative to the edge energy) was included in the fit to minimize the contributions of multiple scattering on the fit. The fit shows the catalyst contains 76 ± 3% and 24 ± 3% Cu(0) and Cu(I), respectively. It is worth noting that the ratio of Cu(I) and Al (2.9:1) is significantly larger than unity (assuming all Al in the framework and Cu(I) ion exchanged at all Brønsted acid sites), indicating the presence of other non-ion exchanged Cu(I) species which are resistant to reduction at 573 K. We speculate the presence of copper phyllosilicate over Cu/PMFI, which has been reported to be present on Cu/silica and such Cu species are difficult to be reduced to metallic Cu at 573 K[28]. The presence of ion exchanged Cu species and copper phyllosilicate could modify the acidity of the parent H-PMFI, such as reducing the number of Brønsted acid sites and introducing additional Lewis acid sites due to Cu, which is further explored via pyridine DRIFTS and NH_3-TPD.

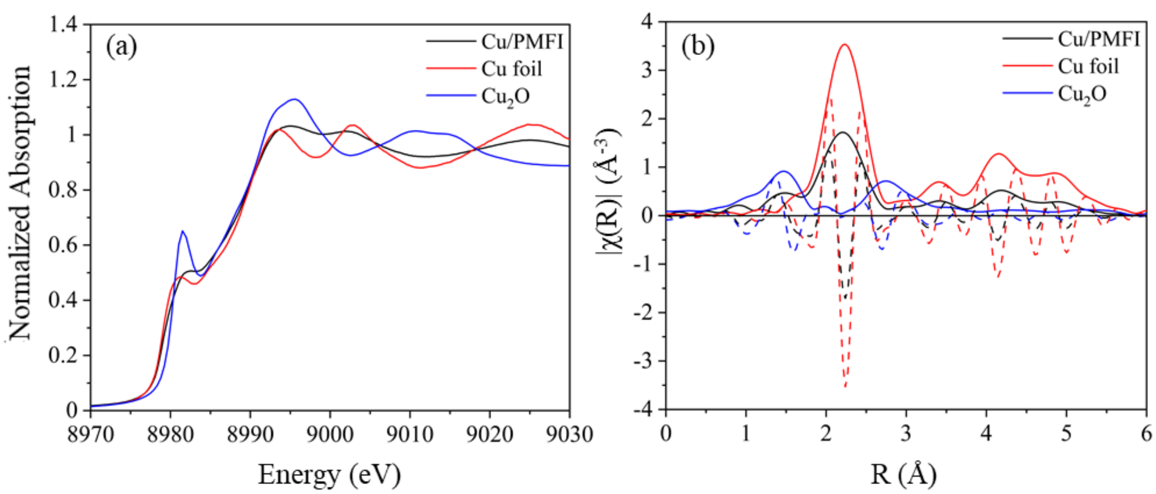

Figure 2. (a) Cu K edge XANES and (b) Magnitude (solid) and real component (dashed) of the Fourier transform of the k^2-weighted EXAFS of the Cu/PMFI catalyst after reduction

at 573 K in 3.5% H_2/He (black), Cu foil (red), and Cu_2O (blue). Detailed fitting parameters are shown in Table S2.

Pyridine DRIFTS was performed to qualitatively understand the type of acid sites over H-PMFI and Cu/PMFI after reduction pretreatment (573 K). For H-PMFI, peaks corresponding to Al-induced Lewis acid and Brønsted acid sites are observed at 1455 cm^{-1} and 1545 cm^{-1} (or 1637 cm^{-1}), respectively (Figure 3)[29]. After loading Cu onto H-PMFI, a new peak at 1450 cm^{-1} arises, likely due to pyridine adsorption over Lewis acidic Cu sites in the form of Cu(I) species as indicated by the XAS analysis. The demolishment of peak at 1637 cm^{-1} implies the possibility of ion exchanging the Brønsted acid sites with Cu sites. NH_3 desorption peaks at both lower (523 K) and higher temperatures (723 K) in NH_3 TPD spectra for Cu/PMFI further indicate the presence of additional acid sites due to the introduction of Cu sites (Figure S5), where similar higher temperature NH_3 desorption peak was observed in Cu modified Beta synthesized by wet impregnation method and Cu modified SSZ-13 zeolites via solid-state ion exchange[30, 31]. Although it is challenging to probe the chemical nature of these new NH_3 adsorption sites, it is clear that loading Cu into H-PMFI modifies the acid properties of the zeolite support by reducing the number of Brønsted acid sites and introducing additional Lewis acid sites.

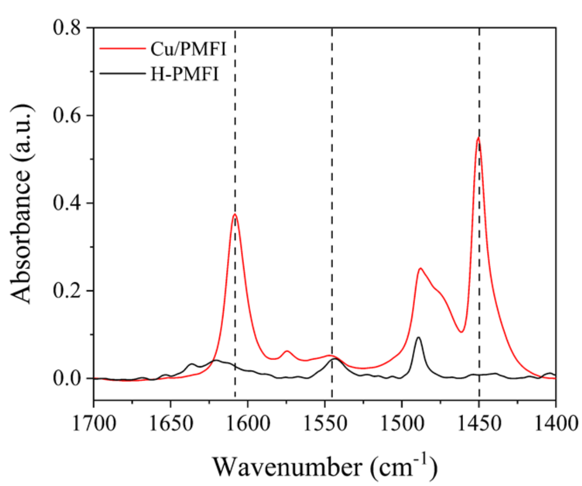

Figure 3. Pyridine DRIFTS study of H-PMFI and Cu/PMFI after pyridine adsorption at 423 K (after calcination at 773 K and reduction at 573 K).

Conversion of 2,3-BDO to Butene-rich Olefins. The Cu/PMFI catalyst was studied for direct 2,3-BDO conversion to butene-rich olefins at 523 K under a hydrogen environment (6.5 kPa 2,3-BDO, 94.8 kPa H_2, WHSV 1.0 h^{-1}). As shown in Table 2, the products include C_2-C_4 alkanes, ethylene, propene, butenes, C_5-C_7 olefins, and methyl ethyl ketone (MEK) with butenes as the major fraction (38-65% butene selectivity during 5-90 hours' time on stream (TOS)) at >96% 2,3-BDO conversion. Four butene isomers (i.e., isobutene, 1-butene, trans-2-butene and cis-2-butene) are observed at all TOS. The types of products observed over this catalyst are similar to other bifunctional catalysts, such as Cu/ZSM-5[12, 14]. The general reaction network of 2,3-BDO conversion to olefins over such bifunctional catalysts[12] has been shown in Scheme 1, reflecting possible reaction sequences leading to the observed products.

Table 2. Conversion and product distributions from 2,3-BDO conversion over Cu/PMFI at different TOS. Reaction conditions: 523 K, WHSV=1.0 h^{-1}, 6.5 kPa 2,3-BDO and 94.8 kPa H_2.

		Product distributions at different TOS			
		5 h	20 h	40 h	90 h
Product selectivities (%)	Ethane	0.1	0.1	0.1	0.0
	Propane	1.1	0.2	0.1	0.0
	Butane	2.3	0.5	0.2	0.2
	Ethylene	0.4	0.0	0.1	0.1
	Propene	9.0	6.4	4.6	3.1
	Isobutene	12	9.5	9.6	11
	1-Butene	6.1	9.5	10	11
	trans-2-Butene	13	22	25	27
	cis-2-Butene	7.1	14	15	16
	Pentenes	29	16	10	6.6
	Hexenes	14	6.7	4.5	3.0

	Heptenes	4.4	3.8	2.1	0.8
	MEK	1.4	12	17	21
	Total butenes	38	55	59	65
	C_{3+} olefins	95	87	81	78
	C_2-C_4 alkanes	3.5	0.7	0.3	0.2
	Others [a]	0.2	0.1	0.3	0.3
Butene isomers ratio [b]		32/16/34/19	17/17/41/25	16/17/41/25	16/17/41/25
2,3-BDO conversion		97	97	97	96

[a] Others include oxygenated molecules like 2-methyl propanal, acetoin, and aromatics (benzene, xylene, toluene); [b] isobutene/1-butene/trans-2-butene/cis-2-butene percentage in total butenes.

Three parallel 2,3-BDO dehydration reactions lead to the formation of MEK (step 1), 2-methyl propanal (MPA) (step 2), and 1,3-butadiene (step 3), respectively. After further hydrogenation and dehydration reactions, butene isomers (i.e., 1-butene, 2-butenes and isobutene) can be produced (step 4-6), which can undergo further oligomerization, cracking and hydrogenation reactions to generate other olefins (such as propene, and C_5-C_7 olefins) and light paraffins (e.g., ethane, propane, and butanes).

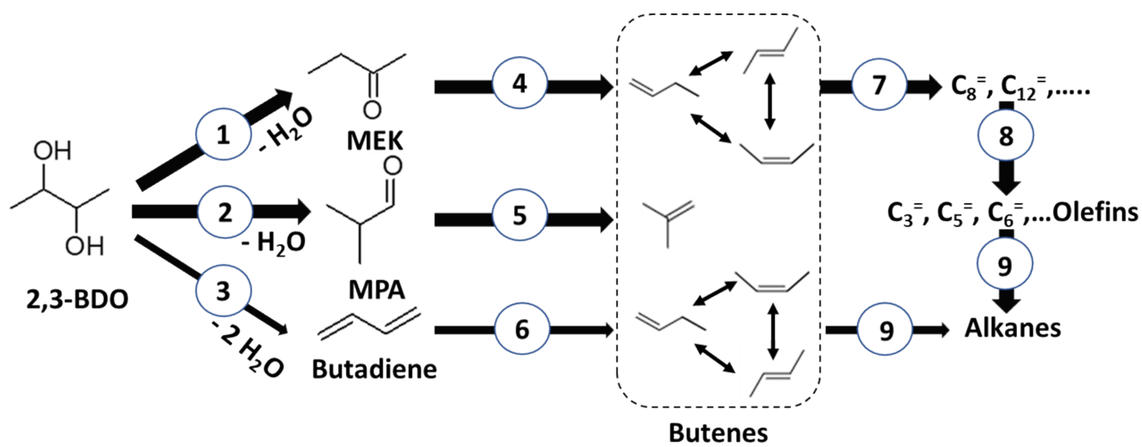

Scheme 1. Proposed reaction network of 2,3-BDO conversion to butene-rich C_{3+} olefins[12].

Selectivities towards different 2,3-BDO dehydration products can be impacted significantly by the choice of catalysts. In this study with Cu/PMFI in the presence of H_2, we primarily observe MEK without seeing other significant dehydration products (i.e., MPA and 1,3-butadiene) at all TOS (Table 2). To further identify other dehydration products, we performed a control experiment with Cu/PMFI operating under Ar instead of H_2 at 523 K to prevent/minimize downstream hydrogenation of the dehydrated products. Consistent with the reaction under H_2, MEK is still the major dehydration product while significant MPA is also observed (e.g., 53% MEK and 16% MPA at TOS =1.5 h, Figure 4); however, there is no 1,3-butadiene in the products, likely suggesting reaction step 1 and 2 are the primary 2,3-BDO dehydration reactions over Cu/PMFI. Furthermore, this also highlights the importance of H_2 in the formation of olefins as reflected in the low butene selectivity (<6%) without H_2.

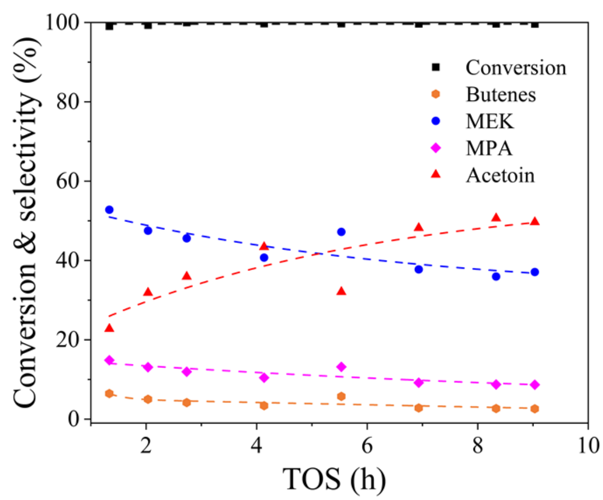

Figure 4. 2,3-BDO conversion and product selectivities over Cu/PMFI. Reaction conditions: 523 K, WHSV=1.0 h^{-1},6.5 kPa 2,3-BDO balanced with 94.8 kPa Ar. The dash lines are used to guide the eye.

These dehydration products, MEK and MPA, can be further hydrogenated to 2-butanol and 2-methyl-1-propanol, respectively, over copper sites under hydrogen. Due to the complexity of different Cu species over Cu/PMFI, it is still challenging to probe the active Cu sites, a potential topic for future investigations. Another series of dehydration steps are followed to further convert 2-butanol to 1-butene and 2-butenes, and convert 2-methyl-1-propanol to isobutene. The fact that we did not observe any alcohols suggests the dehydration steps are very fast over Cu/PMFI under our reaction conditions, consistent with the observations on Cu/ZSM-5(140)[32]. To understand the origin of various butenes, control experiment with direct feeding of 1-butene was performed over Cu/PMFI (Figure 5). 2-Butenes are the predominant products with trace amount of isobutene (selectivity <0.4%), indicating that the isomerization between 1-butene and 2-butenes is possible under our BDO reaction conditions, however, isobutene is not generated via isomerization of either 1-butene or 2-butenes, instead hydrogenation of MPA followed by dehydration is likely the major route to isobutene. Non-butene C_{3+} olefins (e.g., propene, pentenes, hexenes and heptenes) are also formed when directly feeding 1-butene, suggesting butenes are subjected to further oligomerization reactions (step 6) and cracking reactions (step 8) to form other non-butene olefins over Cu/PMFI.

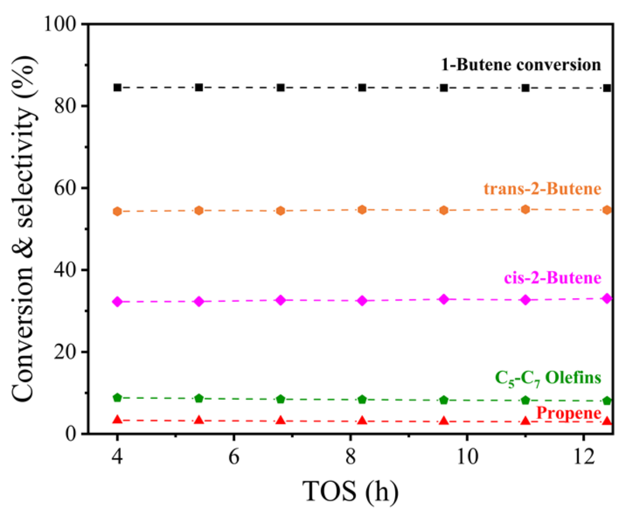

Figure 5. 1-Butene conversion and product selectivities over Cu/PMFI, 523 K, 24.5 kPa H_2, 1.0 kPa 1-butene, and 103.4 kPa N_2. iso-Butene selectivity is below 0.4% and not shown in the figure. The dash lines are used to guide the eye.

Optimization of Butene-rich Olefin Products. As shown in Scheme 1, 2,3-BDO conversion to butene-rich olefins involves multiple steps, where reaction temperature might affect these steps differently so that product selectivities could be varied. Figure 6 (a) shows the impact of reaction temperature on 2,3-BDO conversion and product selectivities at temperature range of 473 and 573 K with all the other reaction conditions maintained constant (6.5 kPa 2,3-BDO, 94.8 kPa H_2, WHSV = 1.0 h^{-1}).

BDO conversions remain above 95% at all studied temperatures, consistent with the observation on Cu/ZSM-5[13] that the BDO dehydration step is very fast. Higher selectivity of MEK is favored at lower reaction temperatures (e.g., 31% MEK selectivity achieved at 473 K). The ratio of MEK and the sum of total olefins and alkanes is used to indicate the extent of hydrogenation of MEK over Cu sites. Continuous decrease of this ratio (0.46 at 473 K, drops to 0.01 at 573 K) suggests hydrogenation activity is promoted at higher temperatures until majority of MEK is converted. Butenes/(total olefins + alkanes) ratio is also chosen to represent the degree of downstream butene oligomerization, cracking and olefin hydrogenation reactions. As shown in Figure 6 (a), this ratio keeps decreasing as temperature increases from 473 to 553 K, indicating these downstream reactions are promoted at above 473 K. Interestingly, this ratio does not decrease further once the temperature is above 553 K. Butene selectivity is balanced by the MEK hydrogenation activity and the downstream oligomerization, cracking and olefin hydrogenation activities, where the optimum butene selectivity (65%) is achieved at 473 K.

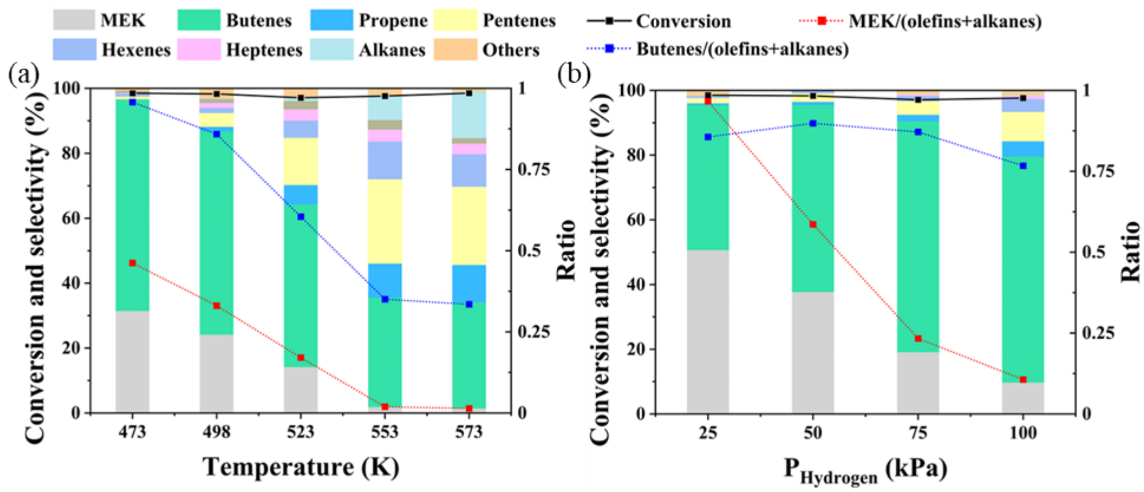

Figure 6. 2,3-BDO conversion, product selectivities and product ratios over Cu/PMFI as a function of (a) reaction temperature at WHSV=1.0 h^{-1}, 6.5 kPa 2,3-BDO balanced with 94.8 kPa H_2 and (b) hydrogen partial pressure at 523 K, WHSV=1.0 h^{-1}, 3.3 kPa 2,3-BDO with total pressure of 101.3 kPa (balanced by Ar). Alkanes include ethane, propane, and butanes. The dash lines are used to guide the eye.

Direct feeding of MEK over Cu/PMFI has shown the reaction is first order with respect to hydrogen partial pressure (Figure S6), indicating the positive influence of hydrogen partial pressure, so we further investigated the impact of hydrogen on 2,3-BDO conversion and product distributions (Figure 6 (b)). The ratio of MEK/(olefins + alkanes) decreases monotonously with increase of hydrogen partial pressure, further confirming the positive effect of hydrogen partial pressure over MEK hydrogenation. The maximum MEK selectivity is observed as 50% at 25% hydrogen partial pressure. The ratio of butenes/(olefins + alkanes) at varied hydrogen partial pressure changes to a much less extent compared to the impact of reaction temperature, suggesting the influence of hydrogen partial pressure over downstream oligomerization reaction is minimal.

Impact of Reduced Diffusion Length on Coke Formation and Olefin Selectivities. Pillared MFI is considered a type of diffusion-free zeolite with ~1 nm diffusion length[21] and well-established mesopore interconnectivity. We hypothesized that once butenes form during 2,3-BDO conversion over Cu/PMFI, they can more readily leave the micropores, enter the mesopores and exit from the zeolite particles in comparison with those mesoporous ZSM-5 catalysts prepared by the post-synthetic desilication method. Thus, further downstream oligomerization and cracking reactions that lead to other olefins can be minimized and larger molecules serving as coke precursors can leave the pores more easily, potentially leading to less coke formation.

For the purpose of understanding the impact of shorter diffusion length on 2,3-BDO conversion to olefins reaction, we synthesized a mesoporous Cu/ZSM-5 as a reference sample using the same ammonia evaporation method and with similar Cu loading (Table S3). This method was chosen in order to simultaneously generate the mesopores and load Cu in one synthesis. N_2 adsorption isotherm analysis indicates the parent H-ZSM-5 has a type I isotherm, consistent with conventional microporous MFI, while it is interesting to note Cu/ZSM-5 has a type IV isotherm with an obvious hysteresis loop (Figure S7). The change of isotherm indicates the formation of mesopores (mesopore volume increase from 0.10 to 0.33 cm^3 g^{-1}, Table S3) when loading Cu onto the support using the ammonia evaporation method, while the micropore volume decreases from 0.17 to 0.08 cm^3 g^{-1}. Interestingly, the STEM analysis (Figure 7 and Figure S8) shows that Cu-ZSM-5 particles have hollow morphology with wall thickness primarily around 30-60 nm. The hollow structure is probably generated by dissolving part of zeolite structure during the ammonia evaporation synthesis. Ammonia solution itself is not effective for post-synthetic desilication[33], so it is likely that the presence of Cu^{2+} ions promotes such dissolution in the presence of ammonia hydroxide. Both lattice features and mesopores on the wall can be clearly observed (Figure 7 (d)). It is worth noting that even large fraction of the core is dissolved, the overall SAR does not change dramatically (Table S3). Pyridine DRIFTS and NH_3 TPD analyses confirmed similar changes of the acid sites during Cu loading onto H-ZSM-5 (Figure S5 and S9) as Cu/PMFI. In summary, Cu/ZSM-5 was prepared as a reference mesoporous material (with post-synthetic method) that has longer diffusion path length than Cu/PMFI due to the larger wall thickness (30-60 nm).

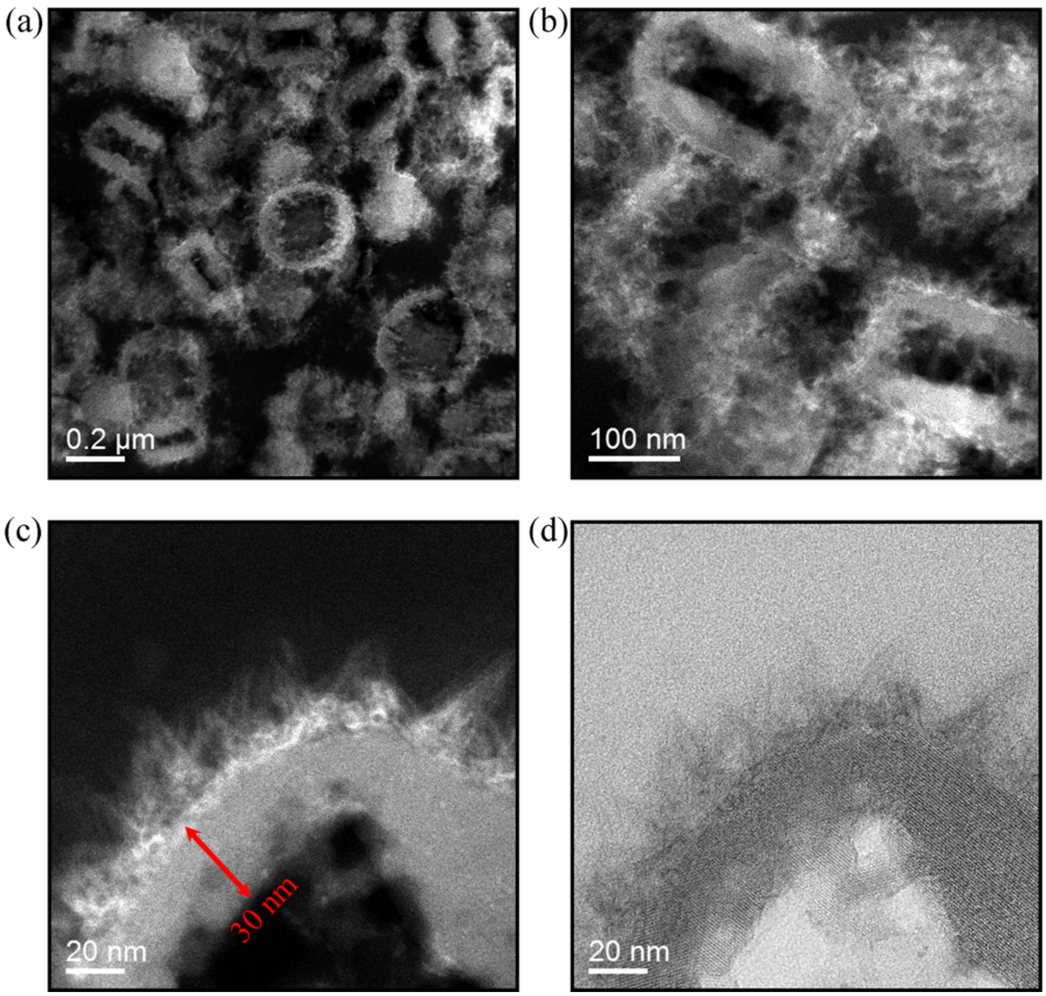

Figure 7. (a-c) Dark-field and (d) bright-field STEM images of as-synthesized Cu/ZSM-5.

Cu/ZSM-5 was evaluated for 2,3-BDO conversion at the same reaction condition as Cu/PMFI (523 K, 6.4 kPa 2,3-BDO, 94.9 kPa H_2, WHSV=1.0 h^{-1}) for ~90 h TOS and the product distributions are shown in Figure S10. Similar types of products are observed over both catalysts, primarily C_{3+} olefins (i.e., propene, butenes, pentenes, hexenes) and MEK. Total C_{3+} olefin selectivity is favored over Cu/PMFI (95% over Cu/PMFI vs 80% over Cu/ZSM-5 at ~5.1 h TOS) and MEK selectivity is relatively low (1.4% over Cu/PMFI vs 19% over Cu/ZSM-5 at ~5.1 h TOS). Coke formation on the spent samples was analyzed with TGA (Figure 8). For both catalysts, coke formation is faster at earlier TOS and then slow down, especially for Cu/PMFI, where 3.1% coke formation is observed for the first 20 h and only an additional 0.6% coke detected in the next 70 h. Coke formation is likely to affect the acid sites for downstream butene oligomerization and cracking reactions as the butene/(olefins+alkanes) ratio increases quickly in the first 20-30 h and slow down after that (Figure S11). It is worth noting that the butene/(olefins+alkanes) ratio on Cu/PMFI increases much slower than Cu/ZSM-5. Direct comparison of coke formation over Cu/ZSM-5 and Cu/PMFI confirms Cu/PMFI can significantly reduce the coke formation (58% coke reduction for spent samples after 90 h TOS), which is very likely due to the reduced diffusion length on 2D PMFI.

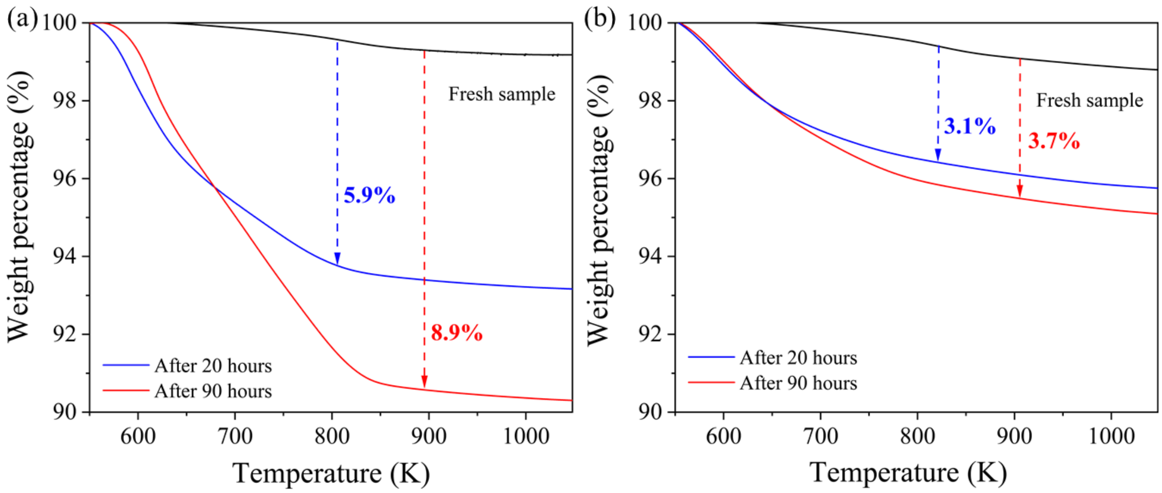

Figure 8. TGA analysis of (a) Cu/ZSM-5 and (b) Cu/PMFI after 2,3-BDO conversion for 20 h and 90 h TOS. Reaction conditions: 523 K, WHSV=1.0 h^{-1}, 6.5 kPa 2,3-BDO balanced with 94.8 kPa H_2.

In order to further evaluate the impact of diffusion length on olefin selectivities, we directly fed MEK (main dehydration product from 2,3-BDO) over Cu/PMFI and Cu/ZSM-5, and control the MEK conversions at a similar medium range (31% to 57%) for both catalysts, for the purpose of understanding the differences in the downstream oligomerization reaction (Figure 9). We did not observe 2-butanol since the dehydration reaction is very fast as discussed above, instead primarily butenes and further downstream products (C_3 and C_{5+} olefins) are obtained. Over Cu/PMFI, MEK conversion is initially 57% and then gradually decreases and stabilizes at ~43% at ~5 h. The primary products are butenes (~99% selectivity, 0.17 h), while the selectivities of propene, pentenes, hexenes and heptenes are all below 0.5%, indicating very minor oligomerization and cracking over Cu/PMFI. MEK conversion over Cu/ZSM-5 starts at ~31%, and gradually increases and stabilizes at ~42%. Although butenes are still the primary products, the overall selectivity is lower than that over Cu/PMFI (77% vs ~99% over Cu/ZSM-5 at 0.17 h). The total selectivity of non-butene C_{3+} olefins over Cu/ZSM-5 is ~21% at 0.17 h and stabilizes at

~9% at ~5 h, much higher than that over Cu/PMFI (~0.7% at both 0.17 h and 5 h). The reduced diffusion length over Cu/PMFI is very likely the reason for the reduced downstream oligomerization/cracking reactions although we cannot completely eliminate the influence of acid sites. The presence of multiple types of acid sites, different acid strength and likely different acid site distributions make it challenging to decouple the impact of acid sites from the diffusion impact.

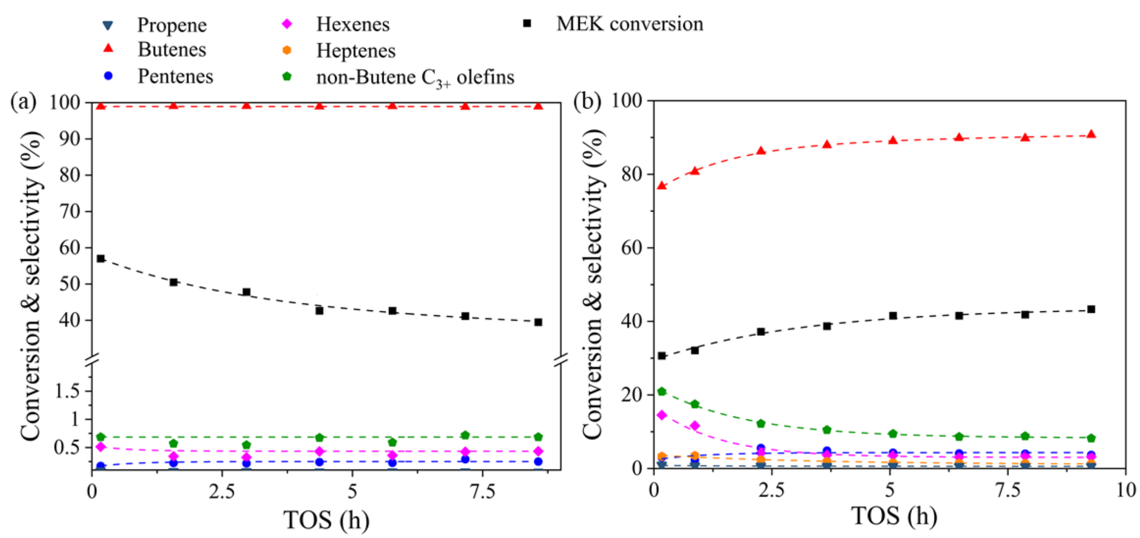

Figure 9. MEK conversion and product selectivity on (a) Cu/PMFI at 503 K, MEK space velocity 21.9 h^{-1}, 3.3 kPa MEK, 34.4 kPa H_2 and 63.5 kPa Ar and (b) Cu-ZSM-5 at 503 K, MEK space velocity 3.1 h^{-1}, 3.3 kPa MEK, 34.4 kPa H_2 and 63.5 kPa Ar. The lines are used to guide the eye.

In summary, the unique mesopore structure in Cu/PMFI brings two benefits for 2,3-BDO conversion, i.e., significantly reduced coke formation and minimizing non-butene olefin formation. Further, butenes formed from BDO can also more easily leave the pores before further oligomerization and cracking to form other olefins, as reflected in the lower non-butene olefin selectivity over Cu/PMFI. Larger coke precursor molecules are more likely to leave the pores in Cu/PMFI, leading to less coke formation.

Conclusions

We have demonstrated a Cu modified diffusion-free 2D pillared MFI catalyst for selective conversion of 2,3-BDO to butene-rich C_{3+} olefins. This catalyst has multiple types of Cu species (e.g., Cu nanoparticles, ion-exchange copper species) and both Brønsted and Lewis acid sites, which can catalyze hydrogenation and dehydration reactions that enable cascade conversion of 2,3-BDO to butenes. Additional oligomerization, cracking and olefin hydrogenation reactions lead to other non-butene olefins and alkanes. Reaction temperature is found to influence the C_{3+} olefin selectivity and olefin composition due to the impact on MEK hydrogenation, downstream oligomerization, and cracking reactions. Hydrogen partial pressure is shown to have a positive impact on MEK hydrogenation, where varying hydrogen partial pressure can be used to tune the ratio of MEK/(olefins + alkanes). Cu modified mesoporous H-ZSM-5 was used as the reference sample which has increased diffusion path length compared to Cu/PMFI. The reduced diffusion length due to much smaller thickness of microporous MFI layers over Cu/PMFI leads to dramatic suppression of coke formation and enhanced butene formation.

ASSOCIATED CONTENT

Supporting Information

The supporting information is available free of charge at https://pubs.acs.org/doi/xxx

XRD patterns; N_2 adsorption-desorption isotherms analysis; STEM images and EDX mapping; H_2-TPR; NH_3 TPD; MEK conversion rates as a function of hydrogen partial pressure; Pyridine DRIFTS; additional product selectivity plots; change of butenes to (olefins + alkanes) ratio; pore volumes of H-PMFI, Cu/PMFI, H-ZSM-5, and Cu/ZSM-5; EXAFS and XANES fitting results; physical and chemical properties of H/ZSM-5 and Cu/ZSM-5.

AUTHOR INFORMATION

***Corresponding author**

E-mail address: liz3@ornl.gov

Author contributions

The manuscript was written through contributions of all authors. All authors have given approval to the final version of the manuscript. [#]Shiba Adhikari and Junyan Zhang contributed equally.

Funding Sources

This research is sponsored by the U.S. Department of Energy (DOE), Office of Energy Efficiency and Renewable Energy, BioEnergy Technologies Office, under contract DE-AC05-00OR22725 with UT-Battelle, LLC, and in collaboration with the Chemical Catalysis for Bioenergy (ChemCatBio) Consortium, a member of the Energy Materials Network. Argonne National Laboratory's work was supported by the U.S. Department of Energy, Office of Energy Efficiency and Renewable Energy, Bioenergy Technologies Office, under contract DE-AC02-06CH11357. This work used the resources of the Advanced Photon Sources, which is a U.S. Department of Energy, Office of Science User Facility supported under contract DE-AC02-06CH11357. MRCAT operations are supported by the Department of Energy and its member institutions. A portion of the research was conducted at Center for Nanophase Materials Sciences, a US DOE Office of Science User Facility. The views and opinions of the authors expressed herein do not necessarily state or reflect those of the United States Government or any agency thereof.

Notes

Patent application is pending for the inventors J. Z., K.A.U. and Z.L.

ACKNOWLEDGMENTS

The authors acknowledge Mohammed Almafrachi for assistance with the small-angle XRD measurement.

References

1. Bender, M., An Overview of industrial processes for the production of olefins–C4 hydrocarbons. *ChemBioEng Rev.* **2014,** *1* (4), 136-147. https://doi.org/10.1002/cben.201400016.
2. Lin, L.; Sheveleva, A. M.; da Silva, I.; Parlett, C. M.; Tang, Z.; Liu, Y.; Fan, M.; Han, X.; Carter, J. H.; Tuna, F., Quantitative production of butenes from biomass-derived γ-valerolactone catalysed by hetero-atomic MFI zeolite. *Nat. Mater.* **2020,** *19* (1), 86-93. https://doi.org/10.1038/s41563-019-0562-6.
3. Yun, G.N.; Ahn, S.J.; Takagaki, A.; Kikuchi, R.; Oyama, S. T., Hydrodeoxygenation of γ-valerolactone on bimetallic NiMo phosphide catalysts. *J. Catal.* **2017,** *353*, 141-151. https://doi.org/10.1016/j.jcat.2017.07.006.
4. Bond, J. Q.; Alonso, D. M.; Wang, D.; West, R. M.; Dumesic, J. A., Integrated catalytic conversion of γ-valerolactone to liquid alkenes for transportation fuels. *Science* **2010,** *327* (5969), 1110-1114. https://doi.org/10.1126/science.1184362.
5. Cordon, M. J.; Zhang, J.; Purdy, S. C.; Wegener, E. C.; Unocic, K. A.; Allard, L. F.; Zhou, M.; Assary, R. S.; Miller, J. T.; Krause, T. R., Selective Butene Formation in Direct Ethanol-to-C_{3+}-Olefin Valorization over Zn–Y/Beta and Single-Atom Alloy Composite Catalysts Using In Situ-Generated Hydrogen. *ACS Catal.* **2021,** *11*, 7193-7209. https://doi.org/10.1021/acscatal.1c01136.
6. Yuk, S. F.; Lee, M.S.; Collinge, G.; Zhang, J.; Padmaperuma, A. B.; Li, Z.; Polo-Garzon, F.; Wu, Z.; Glezakou, V.A.; Rousseau, R., Mechanistic Understanding of Catalytic Conversion of Ethanol to 1-Butene over 2D-Pillared MFI Zeolite. *J. Phys. Chem. C* **2020,** 124, 52, 28437–28447. https://doi.org/10.1021/acs.jpcc.0c05585.
7. Lepore, A. W.; Li, Z.; Davison, B. H.; Foo, G.-S.; Wu, Z.; Narula, C. K., Catalytic dehydration of biomass derived 1-propanol to propene over M-ZSM-5 (M= H, V, Cu, or Zn). *Ind. Eng. Chem. Res.* **2017,** *56* (15), 4302-4308. https://doi.org/10.1021/acs.iecr.7b00592.
8. John, M.; Alexopoulos, K.; Reyniers, M.-F.; Marin, G. B., Effect of zeolite confinement on the conversion of 1-butanol to butene isomers: mechanistic insights from DFT based microkinetic modelling. *Catal. Sci. Technol* **2017,** *7* (14), 2978-2997. https://doi.org/10.1039/c7cy00536a.
9. Sun, J.; Baylon, R. A.; Liu, C.; Mei, D.; Martin, K. J.; Venkitasubramanian, P.; Wang, Y., Key roles of Lewis acid–base pairs on $Zn_xZr_yO_z$ in direct ethanol/acetone to isobutene conversion. *J. Am. Chem. Soc.* **2016,** *138* (2), 507-517. https://doi.org/10.1021/jacs.5b07401.

10. Białkowska, A. M., Strategies for efficient and economical 2, 3-butanediol production: new trends in this field. *World J. Microbiol. Biotechnol.* **2016,** *32* (12), 1-14. https://doi.org/10.1007/s11274-016-2161-x.
11. Köpke, M.; Mihalcea, C.; Liew, F.; Tizard, J. H.; Ali, M. S.; Conolly, J. J.; Al-Sinawi, B.; Simpson, S. D., 2, 3-Butanediol production by acetogenic bacteria, an alternative route to chemical synthesis, using industrial waste gas. *Appl. Environ. Microbiol.* **2011,** *77* (15), 5467-5475. https://doi.org/10.1128/AEM.00355-11.
12. Zheng, Q.; Wales, M. D.; Heidlage, M. G.; Rezac, M.; Wang, H.; Bossmann, S. H.; Hohn, K. L., Conversion of 2, 3-butanediol to butenes over bifunctional catalysts in a single reactor. *J. Catal.* **2015,** *330*, 222-237. https://doi.org/10.1016/j.jcat.2015.07.004.
13. Zheng, Q.; Grossardt, J.; Almkhelfe, H.; Xu, J.; Grady, B. P.; Douglas, J. T.; Amama, P. B.; Hohn, K. L., Study of mesoporous catalysts for conversion of 2, 3-butanediol to butenes. *J. Catal.* **2017,** *354*, 182-196. https://doi.org/10.1016/j.jcat.2017.08.017.
14. Adhikari, S. P.; Zhang, J.; Guo, Q.; Unocic, K. A.; Tao, L.; Li, Z., A hybrid pathway to biojet fuel via 2, 3-butanediol. *Sustain. Energy Fuels* **2020,** *4* (8), 3904-3914. https://doi.org/10.1039/D0SE00480D.
15. Yang, K.; Yan, S.; Sang, Y.; Liu, J.; Yu, L.; Yang, X.; Huang, S., Construction of hierarchical ZSM-5 zeolites by chelating-alkaline medium. *Mater. Today Sustain.* **2021,** *13*, 100070. https://doi.org/10.1016/j.mtsust.2021.100070.
16. Wei, Y.; Parmentier, T. E.; de Jong, K. P.; Zečević, J., Tailoring and visualizing the pore architecture of hierarchical zeolites. *Chem. Soc. Rev* **2015,** *44* (20), 7234-7261. https://doi.org/10.1039/C5CS00155B.
17. Hartmann, M., Hierarchical zeolites: a proven strategy to combine shape selectivity with efficient mass transport. *Angew. Chem. Int. Ed.* **2004,** *43* (44), 5880-5882. https://doi.org/10.1002/anie.200460644.
18. Möller, K.; Bein, T., Mesoporosity–a new dimension for zeolites. *Chem. Soc. Rev* **2013,** *42* (9), 3689-3707. https://doi.org/10.1039/C3CS35488A.
19. Choi, M.; Na, K.; Kim, J.; Sakamoto, Y.; Terasaki, O.; Ryoo, R., Stable single-unit-cell nanosheets of zeolite MFI as active and long-lived catalysts. *Nature* **2009,** *461* (7261), 246-249. https://doi.org/10.1038/nature08288.
20. Na, K.; Choi, M.; Park, W.; Sakamoto, Y.; Terasaki, O.; Ryoo, R., Pillared MFI zeolite nanosheets of a single-unit-cell thickness. *J. Am. Chem. Soc.* **2010,** *132* (12), 4169-4177. https://doi.org/10.1021/ja908382n.
21. Khare, R.; Bhan, A., Mechanistic studies of methanol-to-hydrocarbons conversion on diffusion-free MFI samples. *J. Catal.* **2015,** *329*, 218-228. https://doi.org/10.1016/j.jcat.2015.05.012.
22. Varoon, K.; Zhang, X.; Elyassi, B.; Brewer, D. D.; Gettel, M.; Kumar, S.; Lee, J. A.; Maheshwari, S.; Mittal, A.; Sung, C.Y., Dispersible exfoliated zeolite nanosheets and their application as a selective membrane. *Science* **2011,** *334* (6052), 72-75. https://doi.org/10.1126/science.1208891.
23. Zhang, J.; Lu, Z.; Wu, W.; Tran, D. T.; Shang, W.; Chen, H.; Lei, Y.; Li, Z.; Wang, M.; Woehl, T. J., Mesopore differences between pillared lamellar MFI and MWW zeolites probed by atomic layer deposition of titania and consequences on photocatalysis. *Microporous Mesoporous Mater.* **2019,** *276*, 260-269. https://doi.org/10.1016/j.micromeso.2018.10.009.

24. Shwan, S.; Skoglundh, M.; Lundegaard, L. F.; Tiruvalam, R. R.; Janssens, T. V.; Carlsson, A.; Vennestrøm, P. N., Solid-state ion-exchange of copper into zeolites facilitated by ammonia at low temperature. *ACS Catal.* **2015,** *5* (1), 16-19. https://doi.org/10.1021/cs5015139.
25. Ravel, B.; Newville, M., ATHENA, ARTEMIS, HEPHAESTUS: data analysis for X-ray absorption spectroscopy using IFEFFIT. *J. Synchrotron Radiat.* **2005,** *12* (4), 537-541. https://doi.org/10.1107/S0909049505012719.
26. Wei, Y.; Parmentier, T. E.; de Jong, K. P.; Zecevic, J., Tailoring and visualizing the pore architecture of hierarchical zeolites. *Chem. Soc. Rev.* **2015,** *44* (20), 7234-7261. https://doi.org/10.1039/C5CS00155B.
27. Gawande, M. B.; Goswami, A.; Felpin, F.X.; Asefa, T.; Huang, X.; Silva, R.; Zou, X.; Zboril, R.; Varma, R. S., Cu and Cu-based nanoparticles: synthesis and applications in catalysis. *Chem. Rev.* **2016,** *116* (6), 3722-3811. https://doi.org/10.1021/acs.chemrev.5b00482.
28. Yue, H.; Zhao, Y.; Zhao, S.; Wang, B.; Ma, X.; Gong, J., A copper-phyllosilicate core-sheath nanoreactor for carbon–oxygen hydrogenolysis reactions. *Nat. Commun.* **2013,** *4* (1), 1-7. https://doi.org/10.1038/ncomms3339.
29. Sultana, A.; Nanba, T.; Haneda, M.; Sasaki, M.; Hamada, H., Influence of co-cations on the formation of Cu^+ species in Cu/ZSM-5 and its effect on selective catalytic reduction of NO_x with NH_3. *Appl. Phys. B* **2010,** *101* (1-2), 61-67. https://doi.org/10.1016/j.apcatb.2010.09.007.
30. Widayatno, W. B.; Guan, G.; Rizkiana, J.; Yang, J.; Hao, X.; Tsutsumi, A.; Abudula, A., Upgrading of bio-oil from biomass pyrolysis over Cu-modified β-zeolite catalyst with high selectivity and stability. *Appl. Phys. B* **2016,** *186*, 166-172. https://doi.org/10.1016/j.apcatb.2016.01.006.
31. Clemens, A.; Shishkin, A.; Carlsson, P.-A.; Skoglundh, M.; Martínez-Casado, F.; Matěj, Z.; Balmes, O.; Harelind, H., Reaction-driven ion exchange of copper into zeolite SSZ-13. *ACS Catal.* **2015,** *5* (10), 6209-6218. https://doi.org/10.1021/acscatal.5b01200.
32. Zheng, Q.; Xu, J.; Liu, B.; Hohn, K. L., Mechanistic study of the catalytic conversion of 2, 3-butanediol to butenes. *J. Catal.* **2018,** *360*, 221-239. https://doi.org/10.1016/j.jcat.2018.01.034.
33. Groen, J. C.; Moulijn, J. A.; Pérez-Ramírez, J., Alkaline posttreatment of MFI zeolites. From accelerated screening to scale-up. *Ind. Eng. Chem. Res.* **2007,** *46* (12), 4193-4201. https://doi.org/10.1021/ie061146v.

For Table of Contents Only

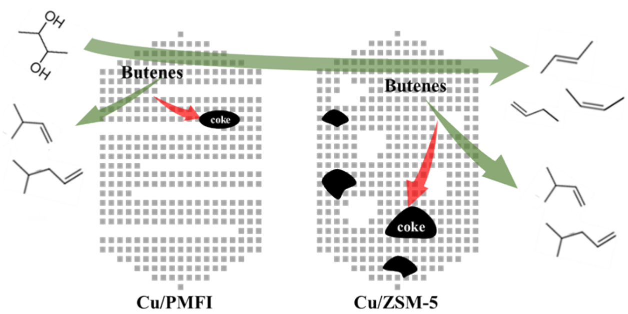

Synopsis:

Diffusion-free pillared MFI based catalyst depresses downstream reactions leading to non-butene olefins and coke formation for 2,3-butanediol conversion.